Electronic Supplementary Material (ESI) for Nanoscale.

Supplemental Information

Flow-directed Synthesis of Spatially Variant Arrays of Branched Zinc Oxide Mesostructures

Abhiteja Konda[a] *and Stephen A. Morin**[ab]

[a]Department of Chemistry, University of Nebraska-Lincoln, Lincoln, NE 68588.

[b]Nebraska Center for Materials and Nanoscience, University of Nebraska-Lincoln, Lincoln, NE 68588.

* To whom correspondence should be addressed. E-mail: smorin2@unl.edu.

I. Materials

The reagents used for the synthesis of ZnO were zinc nitrate hexahydrate (CAS # 10196-18-6), hexamethylenetetramine (CAS # 100-97-0), and ammonium hydroxide (CAS # 1336-21-6) which were purchased from Sigma Aldrich and used as received. The microfluidic stamps were fabricated in PDMS (Sylgard 184®) by Dow Corning Co., purchased from Ellsworth Adhesives and prepared according to manufacturer specifications unless otherwise noted. PET filaments of approximately 23 μm in diameter were purchased from Goodfellow USA. The polymer sheets that were used as supports for the PET filaments were purchased from McMaster-Carr®. Flow to the microfluidic devices was supplied using Tygon®/polyethylene tubing. A MasterFlex L/S peristaltic pump by Cole-Parmer® was used to drive fluid flow. The varieties of tubing used were Masterflex Tygon® Lab E-3603 Tubing purchased from Cole-Parmer®, and Polyethylene tubing, Intramedic™ PE-160 by BD & Co, purchased from Fisher Scientific. PET ribbons were cut from commercially available transparency films (manufactured by 3M).

II. Methods

1. Fabrication of Microreactors and Operation

The microfluidic stamps were fabricated in PDMS in the ratio of 10:1 (base:catalyst). The curing time for PDMS was 90 mins at 70°C. The masters used to make these devices via soft-lithography were fabricated in ABS using a 3D printer (Dimension Elite, Stratasys Ltd.). The PET filaments were attached to a polycarbonate substrate using double-sided tape on either ends, and a microfluidic stamp was sealed to the substrate using a manual compression device.[1] The channels were approximately 1.35 mm x 1.35 mm, and when compressed and sealed over the

PET filament were approximately 840 μm × 700 μm (w × h). We determined the channel dimensions by replicating the channels in epoxy and examining the cross-section using optical microscopy.

Flow to the devices was controlled using peristaltic pumps, and the flow experiments were carried out at room temperature. A range of flow rates (0.5 ml/min to 30 ml/min) were investigated.

2. PET Filaments and Ribbons

The PET filaments were cleaned by rinsing with IPA (the PET ribbons were pre-cleaned by sonicating in Toulene for 10 mins followed by sonicating in deionized water for 5 mins to remove the organic coating before rinsing with IPA), followed by sonication in nanopure water for 10 mins, and then dried in a convection oven at 60°C for 2 hrs. The filaments/ribbons were then suspended on an acrylonitrile butadiene styrene (ABS) holder that was previously coated with PDMS. The PDMS coating prevents leaching of impurities (if any) into the growth solution. The ABS holder was necessary to maintain the orientation of the filaments/ribbons in the growth solution.

3. Growth of ZnO NR Arrays and Branched NR Arrays

Vertical arrays of ZnO NRs were grown on PET filaments (or ribbons) using equimolar concentration of 12.5 mM zinc nitrate hexahydrate and hexamethylenetetramine (HMT) for 2.75 hrs at 95°C in centrifuge tubes previously cleaned by rinsing with IPA and nanopure water. The PET filaments/ribbons with the ZnO NR arrays were then rinsed with deionized water and introduced into a microfluidic reactor and exposed to precursor solutions of 2 mM zinc nitrate

hexahydrate and 0.14% ammonium hydroxide, which resulted in secondary growth "branches" on the NRs in the exposed regions. We observed no secondary growth in the absence of flow or under low-flow otherwise identical conditions (Fig. S3).

We used zinc nitrate salt and ammonium hydroxide to achieve the secondary growth at room temperature.[2] We observed and analyzed multiple branched NRs using TEM and HRES-TEM to verify the "quasi-epitaxial" growth relationship between the trunk and the branches (Fig. 2 and Fig. S5). The SAED patterns were collected from the center for the branches and at the edge/tip of the trunks (to avoid potential contribution from branches out of view) for the trunks resulting in relatively low intensity signals (Fig. 2bi). The patterns were analyzed using the SAED2s module of the Landyne software suite.[3] To understand the growth mechanism of secondary branches, we exposed the filaments with ZnO NR arrays to precursor solutions for different durations: 45, 60, 75, and 90 minutes (Fig. S6). The SEM images indicated the formation of a polycrystalline layer initially for about 45-60 mins with no (or minimal) branching up until 60 minutes, while the images for 75 and 90 mins show branching. The growth of the polycrystalline layer is independent of the flow rate; we see no/few branches after one hour regardless of the flow rate (Fig. S7).

For the PET ribbons, we expect relatively long branches and that the difference in length from the leading to the trailing edge would be relatively less, when compared to filaments processed under similar conditions. This difference comes from the vertical height of the PET ribbons (~60 μm taller than the filaments) which positions the NR array higher in the channel, thus exposing the array to higher flow velocities which in turn suppressed the stagnant layer and led to higher growth rates and longer branches (Fig. S2).

4. Flow Parameters

a. Velocity

We used flow rates of 5, 10, 20, 25, and 30 mL/min. We use dual pump heads to eliminate the pulsation in the channels. The two precursor solutions were flowed at equal flow rates, and were combined using a Y-connector just before the inlet (to minimize reaction in the tubing) of the microfluidic reactor resulting in the desired final flow rate. We then estimated the linear flow velocity, which can be given by:[4]

$$velocity,\ \bar{\upsilon} = \frac{Q}{(H)^2} \tag{1}$$

where Q is the flow rate, and H is the hydraulic diameter of the channel. For a rectangular channel H is given by $\frac{2\,l\,b}{l+b}$, l is the length and b is the breadth of the channel.

While $\bar{\upsilon}$ is the linear flow velocity at the center of the channel, we can also estimate the velocity at a given point in the channel (for example, at the filament edge), using the following expressions:

$$u_c = u_{max}\left(1 - \frac{y^2}{h^2}\right) \tag{2}$$

$$u_c = \frac{3}{2}\bar{\upsilon}\left(1 - \frac{y^2}{h^2}\right) \tag{3}$$

where u_{max} is the maximum velocity in the channel and is given by $\frac{3}{2}\bar{\upsilon}$, y is the distance between the point at which the velocity is being measured and the center of the channel, and h is half the hydraulic diameter.

We estimated the linear flow velocities to be 14.2×10^{-2}, 28.3×10^{-2}, 56.7×10^{-2}, 70.9×10^{-2}, and 85.0×10^{-2} m/s at the center of the channel, and as 4.6×10^{-2}, 9.2×10^{-2}, 18.3×10^{-2}, 22.9×10^{-2}, and 27.5×10^{-2} m/s at the leading edge of the filament for flow rates of 5, 10, 20, 25, and 30 ml/min respectively.

b. Reynolds Number (Re)

The Reynolds number is a dimensionless parameter that illustrates the flow profile in the channels, and is given by:[5]

$$Re = \frac{L\,\bar{\upsilon}}{\eta} \tag{4}$$

where L is the length of the channel, $\bar{\upsilon}$ is the linear flow velocity, and η is the kinematic viscosity of the fluid (Table S1). The Reynolds numbers for the flow velocities used ranged from 2–34, which indicate a laminar flow regime (see Main Text Fig. 3b).[6]

5. Stagnant Layer Thickness, *d*[7, 8]

We estimated the stagnant layer thickness using the following equation (Table S1):

$$d \cong 5\left(\frac{x\,\eta}{\vartheta\,\rho}\right)^{1/2} \tag{5}$$

We used different flow velocities and plotted it as a function of the distance from the leading edge of the filament (Main Text Fig. 3c). It was clear that d increases as the distance from the leading edge of the filament increased, and that it correspondingly decreased as the flow velocity increased. These relationships are expected from the proportionalities expressed in the eq. 5. The position of the NRs on the filament relative to the flow direction, in combination with

different flow velocities resulted in a predictable stagnant layer thickness and thus control over the extent of secondary branching.

6. Dislocation Driven Growth Rate, R_{DD}[7, 8]

a. Supersaturation, σ

According to the BCF theory,[9] dislocation driven growth dominates crystal growth at low supersaturation. Supersaturation can be given by:

$$\sigma = \ln\left(\frac{c}{c_0}\right) \tag{6}$$

where c is bulk concentration, and c_0 is the equilibrium concentration (Table. S1).[7]

To experimentally determine c_0, we carried out a series of experiments where the ZnO NR arrays were subjected to precursor solutions of different concentrations (Fig. S8). The concentration at which the NRs were in equilibrium with the $Zn(NO_3)_2 \cdot 6H_20$ and NH_4OH system (i.e., where the NRs neither grow nor dissolve) was determined. The concentrations of the precursor solutions investigated ranged from 10 μM to 100 μM for $Zn(NO_3)_2 \cdot 6H_20$ and 0.0007% to 0.007% for NH_4OH. The SEM images showed that the NRs experienced some dissolution at 50 μM and started to grow at 100 μM, which indicated that the equilibrium concentration ranged from 50–100 μM (we therefore used the average, 75 μM in discrete calculations, and both extremes in Fig. 4c of the main text). Using the c_0 (75 μM), we calculated the supersaturation in our system to be 3.3.

b. Growth rate constant, C

We calculated the growth rate constant using the physical constants and variables as listed in Table. S1 using the following equation:

$$C = \frac{D\, c_0\, \vartheta_c}{d} \tag{7}$$

In our system, since the values for $D, c_0,$ and ϑ_c do not change, the growth constant is inversely proportional to the stagnant layer thickness, which depends on the velocity.

c. Dislocation driven growth rate

Assuming that the supersaturation is much higher than the characteristic supersaturation, a linear rate law can be obtained and given by:

$$R_{DD} = C\, \sigma \tag{8}$$

7. Layer-by-layer Growth Rate, R_{LBL}[7, 8]

We also calculated the layer-by-layer growth rate for our system. In LBL growth, an island is nucleated on the surface and the monomer addition takes place at the step-edges until a growth facet is completely covered. This process repeats over and over again, leading to the formation of a crystal. The macroscopic rate law for the LBL growth (R_{LBL}) can be given by:

$$R_{LBL} = J_0 l^2 \beta \tag{9}$$

where J_o is the rate of 2D nucleation, L is the length of the active growth facet (measured by taking the average diameter of the branches from multiple TEM images), and β is the step height (Table S1). In case of solution phase growth the J_o can be expressed as:

$$J_o = vc\vartheta c(\sigma)^{1/2} e^{\left(\frac{-\Delta U}{kT}\right)} N_o e^{\left(\frac{-\pi\epsilon^2 a^2}{k^2 T^2 \sigma}\right)} \quad (11)$$

The value for the surface energy (γ) used to calculate the specific edge energy (ϵ) was estimated to be 0.143 J/m^2 using the equation:[8]

$$\gamma = a^{-2}[12.08 - 1.17\ln(c_0)] \times 10^{-21} \quad (12)$$

The calculated ϵ value of 4.65×10^{-11} J/m, gave an R_{LBL}'s of 2.38 nm/s, which resulted in a predicted length of the branches (4,282 nm) that is very large (~21 times larger) compared to the experimentally measured lengths (197 nm) of the branches grown at 10 ml/min in the transition (TsR) region.

8. Branch density and length measurements

We used the SEM images to analyze the three regions (LR, TsR, and TR) of the filament, which were further divided into three zones. To estimate branch density (number of branches per NR), we counted the total number of the branches in each zone and divided it by the number of NRs in that zone (N>300 NRs per region). We also measured the lengths of the branches (N=75 branches per region) using an image analysis software (ImageJ). When compared, 13 out of the 15 experimentally measured lengths agreed with the theoretically predicted (using macroscopic rate laws) lengths at 95% confidence.

The differences in the predictions from macroscopic rate laws and the experimental measurements can be partly explained by the fact that the measured lengths were an average of the branches on NRs within the growth regions that were approximately 10 μm in width (e.g., 0–10, 10–20, and 20–30 μm) from the leading edge, whereas the macroscopic calculations predicted length for branches at specific distances (e.g., at 10 μm). Additionally, predictions

assumed that the branches started to grow only after 60 mins; however, experimentally it was found that the branches can start to grow any time after 45 mins (assuming the branches start growing at 45 mins, the predicted length had an average deviation of 14% compared to the measured lengths for the five different flow rates, across three regions). As these analyses are based on SEM images, we only included NRs/branches that were in the view, and further, we made every effort to report lengths that were measured for branches that were perpendicular to the imaging axis of the SEM. We also minimized error by collecting data from multiple zones within each region. We also observed branching on the NRs that are on the bottom side of the filament (Fig. S1).

9. Transitional metal doped ZnO branches

We demonstrated the ability to dope ZnO with transition metals (e.g., copper) leading to branched NR arrays with spatially variant *Cu* concentration (Fig. S11). The secondary growth step was modified by doping the ZnO precursor solution with 10% of 2 mM copper nitrate solution, and the solutions were flowed at a rate of 15 ml/min for 2 hrs. We analyzed the Cu-doped ZnO branches quantitatively using Energy Dispersive X-ray Spectroscopy (EDS), and determined the *Cu* concentration in three zones for each region (LR, TsR, and TR). Similar to the previous experiments, we observed a gradient in the atomic % of *Cu* across the filament with a higher % in the LR and a lower % in the TR (Fig. S11). The EDS was performed using a Zeiss EVO MA10 Scanning Electron Microscope at an accelerating voltage of 25 kV and a scan time of 10 mins per zone.

10. X-Ray Diffraction (XRD)

We characterized the ZnO NR arrays with and without branches using XRD (Fig. S4). We used Bruker-AXS D8 Discover with GADDS at 20 cm detector with Cu Kα radiation (λ = 1.5416 Å). The XRD spectra were recorded in the range of $20^{\circ} \leq 2\theta \leq 80^{\circ}$ at a scan rate of 2/hour. For the ZnO NR arrays (Fig. S4a) the peaks at $2\theta = 31.7^{\circ}$, 34.4°, 36.15°, 47.5°, 56.5°, 62.75°, and 67.8° were assigned to (100), (002), (101), (102), (110), (103), and (112); for the ZnO NRs with branches (Fig. S4b) the peaks at $2\theta = 31.65^{\circ}$, 34.35°, 36.2°, 47.5°, 56.5°, 62.75°, and 67.85° were assigned to (100), (002), (101), (110), (103), and (112), both indicating the wurtzite structure (Zincite, international center for diffraction data, ICDD, file no. 04-008-8198). The slight difference in the relative intensities of the peaks is due to the alignment of the NRs on the PET filament with respect to the X-ray beam/source direction.

11. Scanning electron microscopy (SEM) and transmission electron microscopy (TEM)

a. **SEM:** The filaments/ribbons after the secondary growth step are dried by flowing nitrogen through the channels, and were later attached to metallic SEM stubs using double-sided carbon tape. The samples were sputter coated with gold for 21 secs using a Cressington Au sputter coater, and were observed using a FEI Quanta 200 Environmental SEM at an accelerated voltage of 20–30 kV.
b. **TEM:** Samples for TEM were prepared by gently scrapping the NRs from the PET filament onto lacey formvar carbon grids 200 mesh (purchased from Ted Pella Inc.). All the samples were characterized using a JEOL JEM 2010 TEM (for SAED patterns) and FEI Tecnai Osiris (S) TEM (for Hi-Res images) at an accelerating voltage of 200 kV.

12. Precursor concentration profile calculation using COMSOL®

We used COMSOL to generate a concentration profile for the Zn^{2+} species in the precursor solution at a flow rate of 5 ml/min (Fig. S9). The profile illustrates the variation in concentration gradient within the stagnant layer as a function of distance from the leading edge (in μm). The following assumptions/variables were used to generate the map: the bulk concentration is 2 mM, the concentration at the crystal surface is 0 mM, and the diffusion coefficient for Zn^{2+} species is 1×10^{-9} m^2/s (Table S1). We then overlaid the expected branch length (assuming that the branches grew for 30 mins, and an equilibrium concentration of 75 μm) and the measured branch lengths at three positions on the filament following a 5 ml/min secondary growth.

Table S1. Physical constants and variables used for calculations.

Symbol	Definition	Value used
β	Step Height	5.2038×10^{-10} m
c	Bulk concentration	2 mol/m^3
c_0	Equilibrium concentration	0.05 – 0.1 mol/m^3
C	Growth rate constant	variable
d	Stagnant layer thickness	variable
D	Bulk diffusion coefficient	1×10^{-9} m^2/s,[10]
ϵ	Specific Edge Energy = a×γ	4.65×10^{-11} J/m
γ	Surface Energy	0.143 J/m^2,[8,‡]
k	Boltzmann's Constant	1.38065×10^{-23} J/K
l	Nanorod Cross-section	89.7×10^{-9} m*
L	Length of the channel	40 μm[†]
N_o	Absorption site density	1.094×10^{19} 1/m^2,[6]
η	Kinematic viscosity of water	1×10^{-6} m^2/s
ρ	Density of water	1 g/cm^3
Q	Flow rate	5, 10, 20, 25, 30 mL/min
σ	Supersaturation	3.3
T	Temperature	298 K
ΔU	Energy of desolvation	7.29×10^{-20} J,[7]
ν	Monomer collision frequency	1×10^{13} 1/s,[7]
ϑ	Velocity	Variable
ϑ_c	Volume of growth unit	2.86×10^{-5} m^3/mol
x	Distance from the leading edge	0 − 40 μm

‡ estimated using Eq. 12 and a c_0 of 0.075 μM (6)

* average diameter of the branches measured from TEM images

† length that the solution travels; assumed to be equal to the cross-sectional diameter of the filament (Fig. 3a).

Figure S1. Branching around the filament. (a) Schematic showing the six different regions on the filament. (b) SEM images from the regions annotated in panel a. Arrow indicates the flow direction (at a rate of 5 ml/min.).

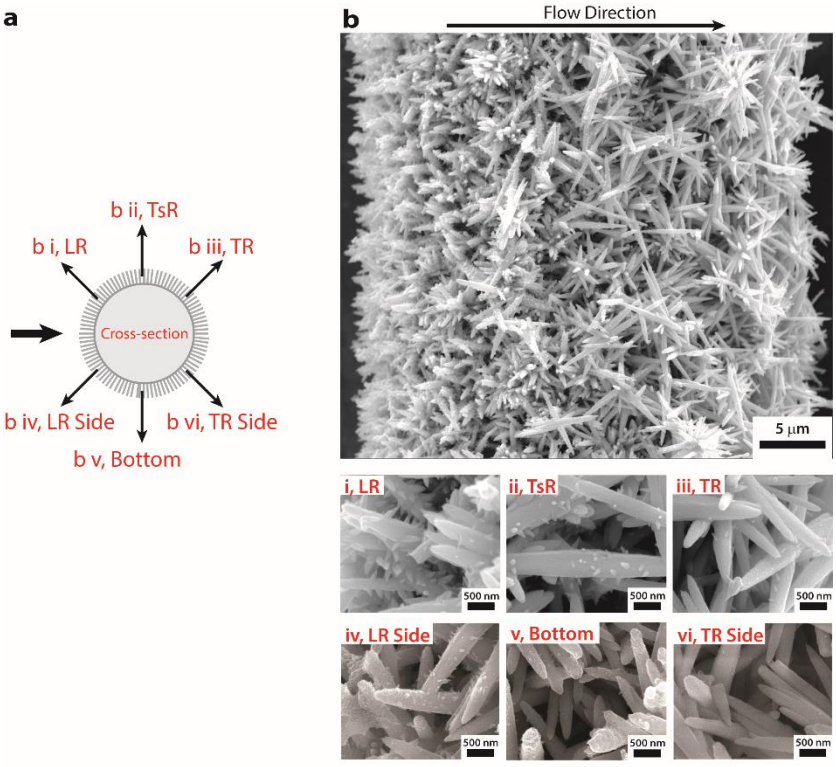

Figure S2. Branched ZnO mesostructures on PET Ribbons. (a) Schematic showing the cross-sectional dimensions of the PET ribbon and zones analyzed. (b) Low magnification scanning electron microscopy (SEM) images of the branched ZnO NR arrays following secondary growth in the microreactor (Fig. 1a main text), where the dashed boxes indicate zones for high-magnification analysis. (c) High-magnification SEM images showing the morphology across the ribbon (i–iii). The location of the high-magnification images are annotated in panel b. The direction of flow is indicated in panel b and the velocity of flow was 10 ml/min.

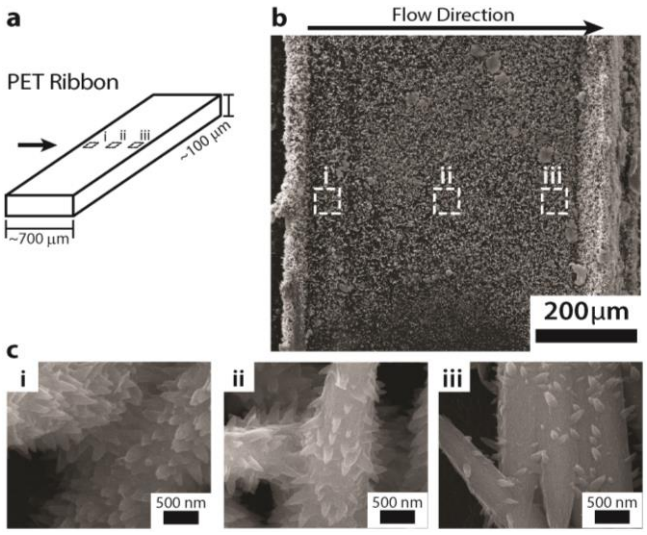

Figure S3. Secondary Growth in the absence of flow and at low flow rates. (a–c) SEM images of the NRs on the PET filaments after exposure to precursor growth solutions in the absence of flow for 1.5 hrs (a), 3 hrs (b), and 6 hrs (c). (d–f) SEM images of the NRs after exposure to precursor solutions under different conditions: a macroscale continuous flow reactor at 0.5 ml/min (d), a microfluidic reactor at 0.5 ml/min (e), and a 40 ml constant volume bath where the growth solution was replaced every 15 minutes (f).

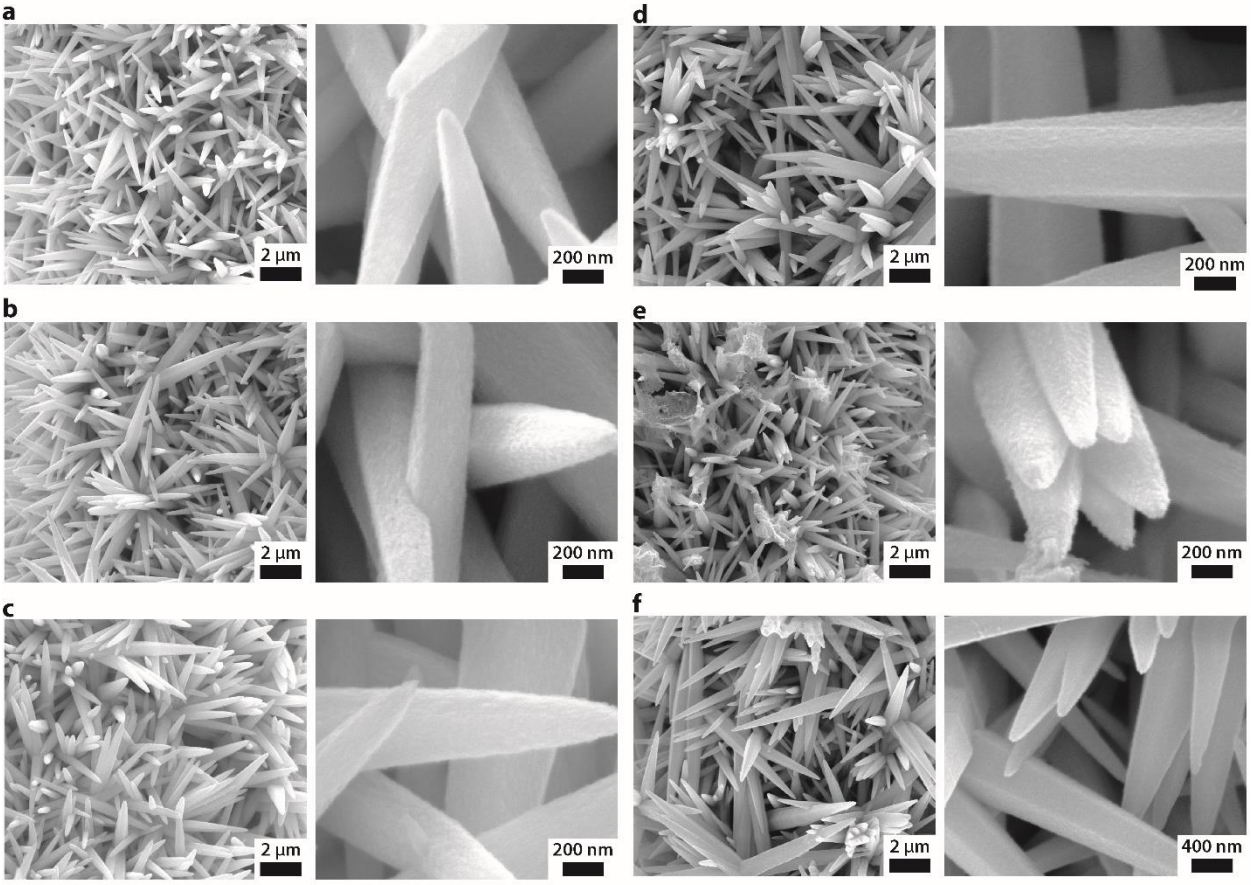

Figure S4. X-ray Diffraction (XRD) of the NR arrays with and without branches. (a-b) XRD for NR arrays after the first growth step (a), and for the branched NRs after the second growth step (b). The bottom insets show the reference data for Zincite, obtained from the International Center for Diffraction Data (ICDD) file no. 04-008-8198.

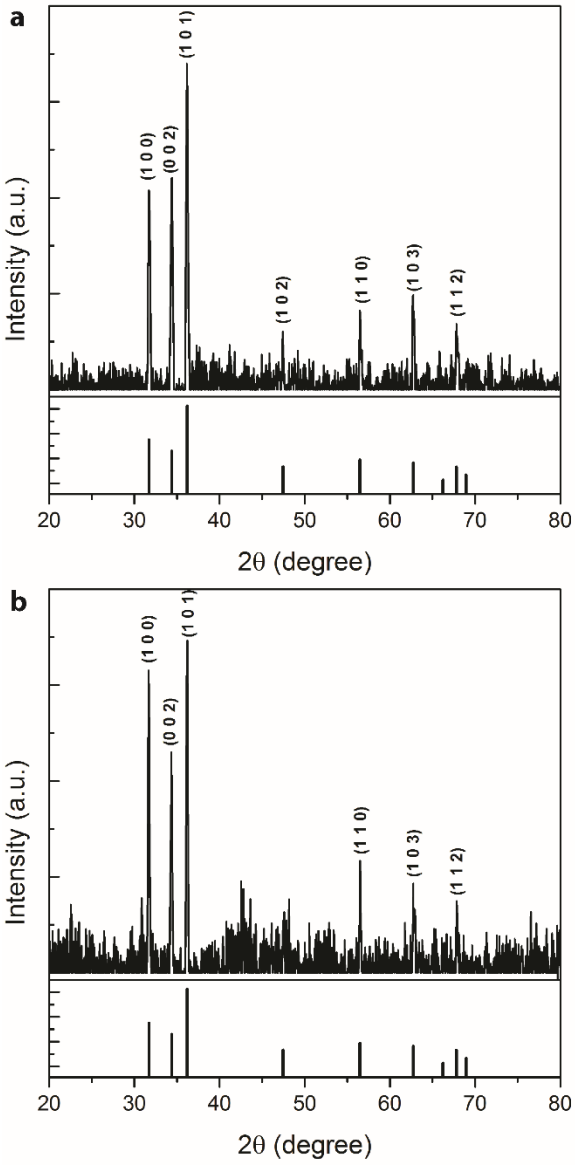

Figure S5. TEM characterization of branched ZnO NRs. (a–c) Three examples of NRs showing the "quasi-epitaxial" growth relationship between the trunk and branches. The SAED patterns (i, ii) and HRES-TEM images (iii, iv) for each panel of the NR indicate that both the trunk and branches grew along the [0 0 2] direction.

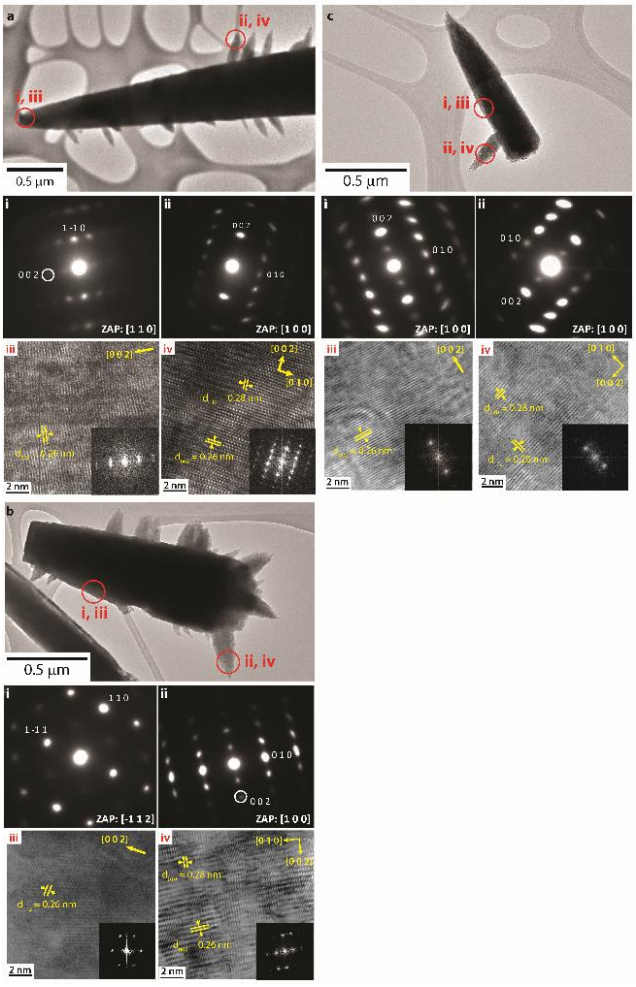

Figure S6. Time evolved branch growth. (a–e) SEM images of the NRs on the PET filaments after exposure to precursor growth solutions at 15 ml/min for 0 min (a), 45 mins (b), 60 mins (c), 75 mins (d), and 90 mins (e). SEM images (f), a TEM image (g), and a HRES-TEM image (h) showing a oriented polycrystalline layer surrounding the ZnO NR with the FFT's (i–iv) verifying its alignment with the underlying NR.

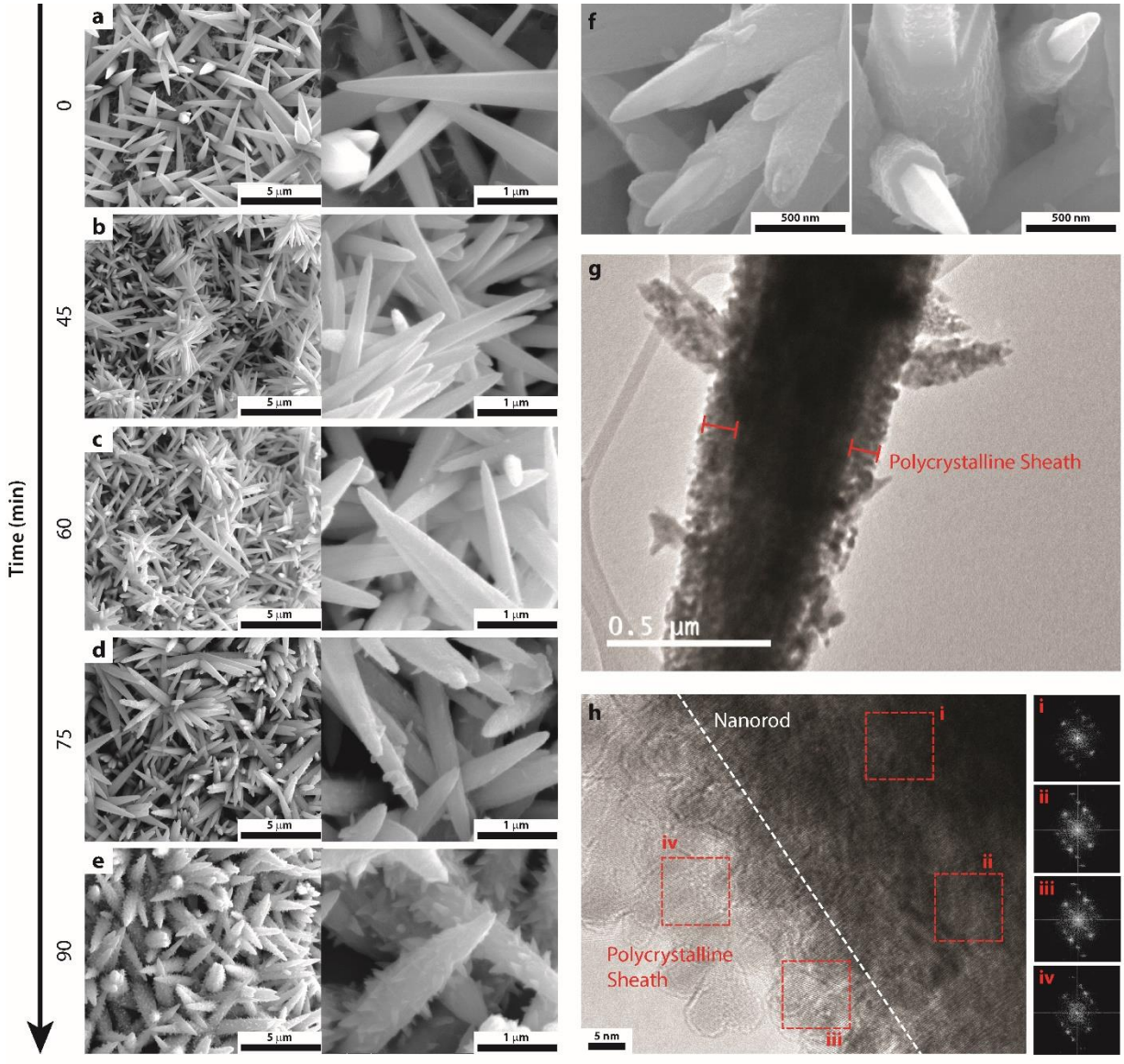

Figure S7. Effect of flow rate on polycrystalline layer. (a–e) The SEM images show the formation of polycrystalline layer and the onset of branch growth at the end of 1 hr for five different flow rates: 5 (a), 10 (b), 20 (c), 25 (d), and 30 (e) ml/min.

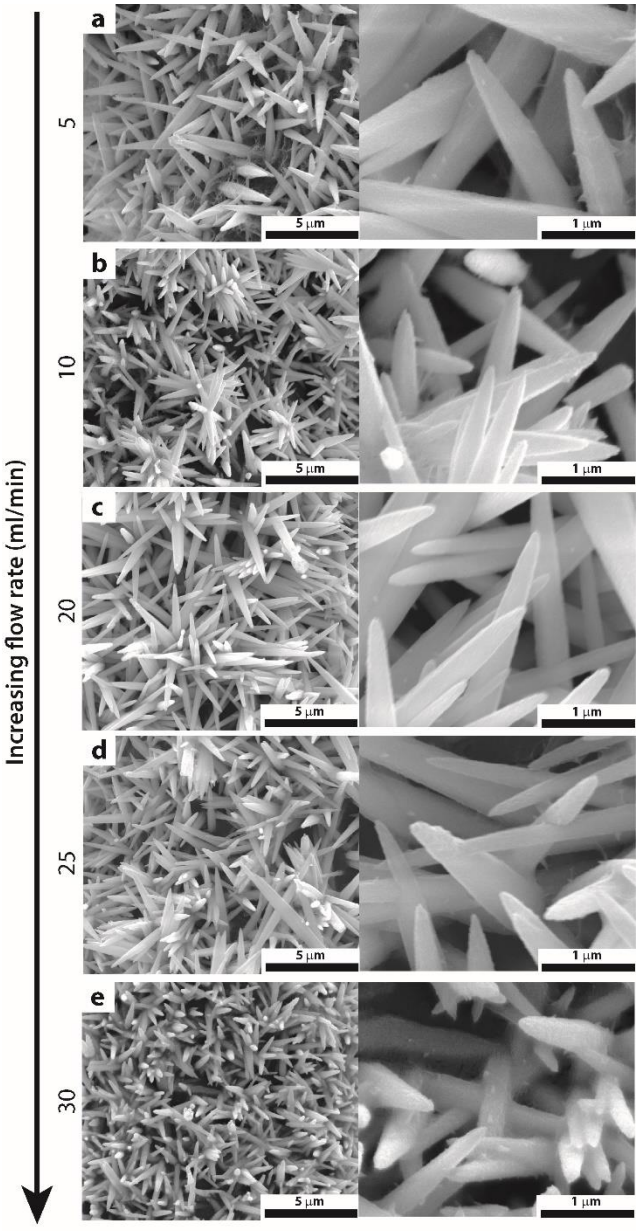

Figure S8. Determination of equilibrium concentration. The SEM images of the branched ZnO NR arrays before (left panel, a–d), and after (right panel, (a'–d') exposing them to precursor solutions of different concentrations for 4 hrs. The dotted line indicates the concentrations of interest—at 50 μM, the branches dissolve, and at 100 μM, they grow, indicating the c_o is approximately between 50–100 μM.

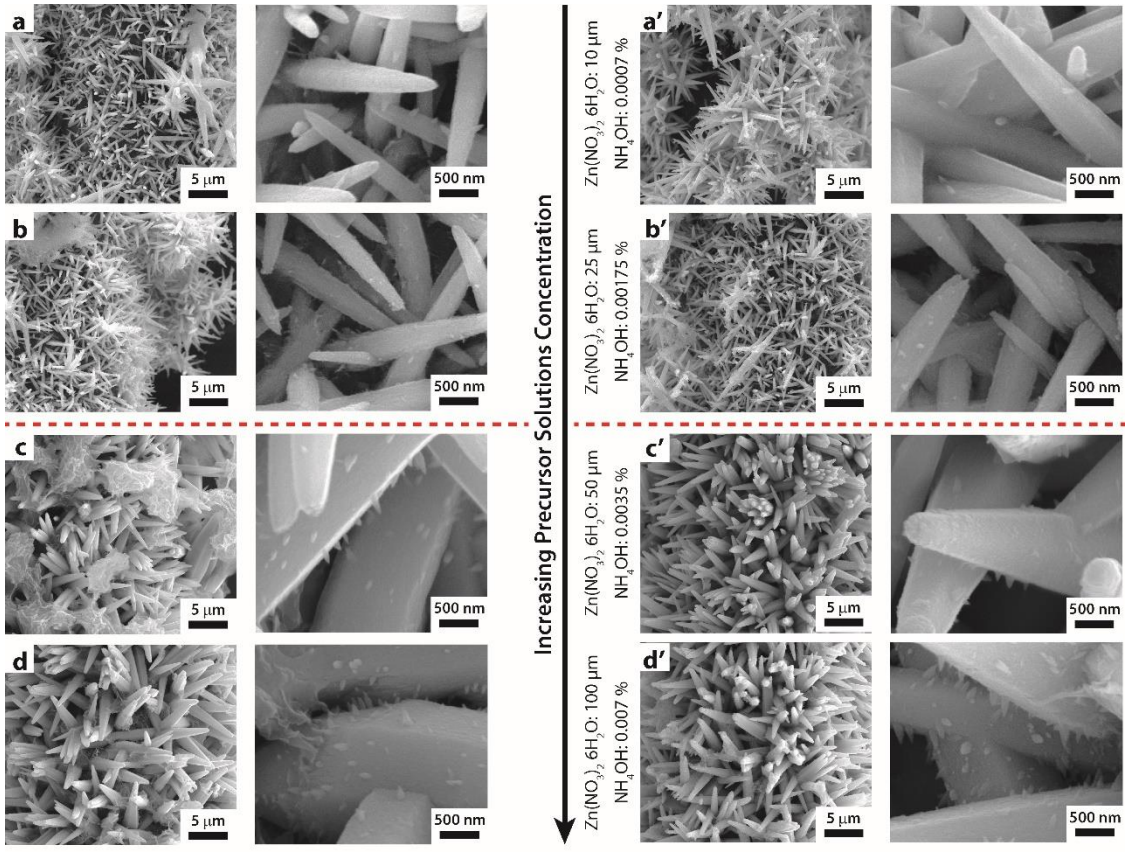

Figure S9. Concentration profile of the Zn^{2+} species in the precursor solution across the filament at a flow rate for 5 ml/min.; the bulk formal concentration of Zn^{2+} = 2.0 mM. The location of the stagnant layer boundary is also indicated (white trace). The calculated (black dashed trace) and the experimentally measured (black boxes) branch lengths are overlaid on the concentration profile.

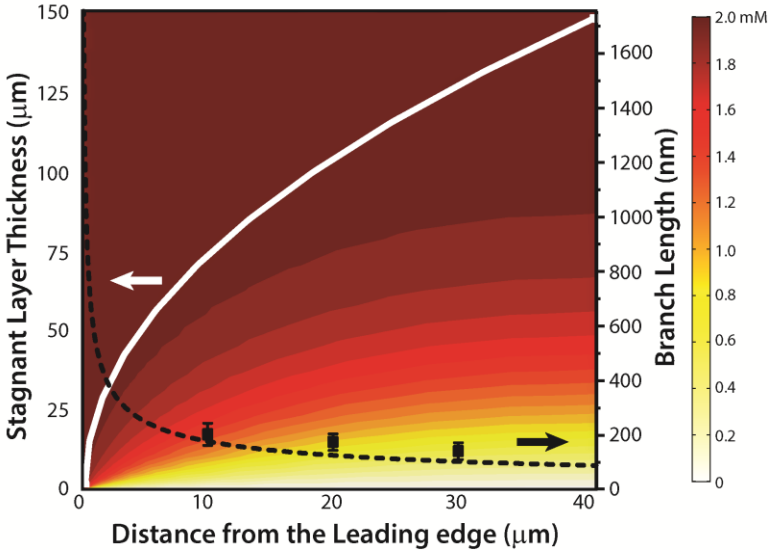

Figure S10. Effect of fluid flow velocity on secondary growth. (a–e) SEM images showing the secondary growth on ZnO NRs at different flow rates (5, 10, 20, 25, and 30 ml/min) in three different regions: leading edge (i), transition region (ii), and trailing edge (iii).

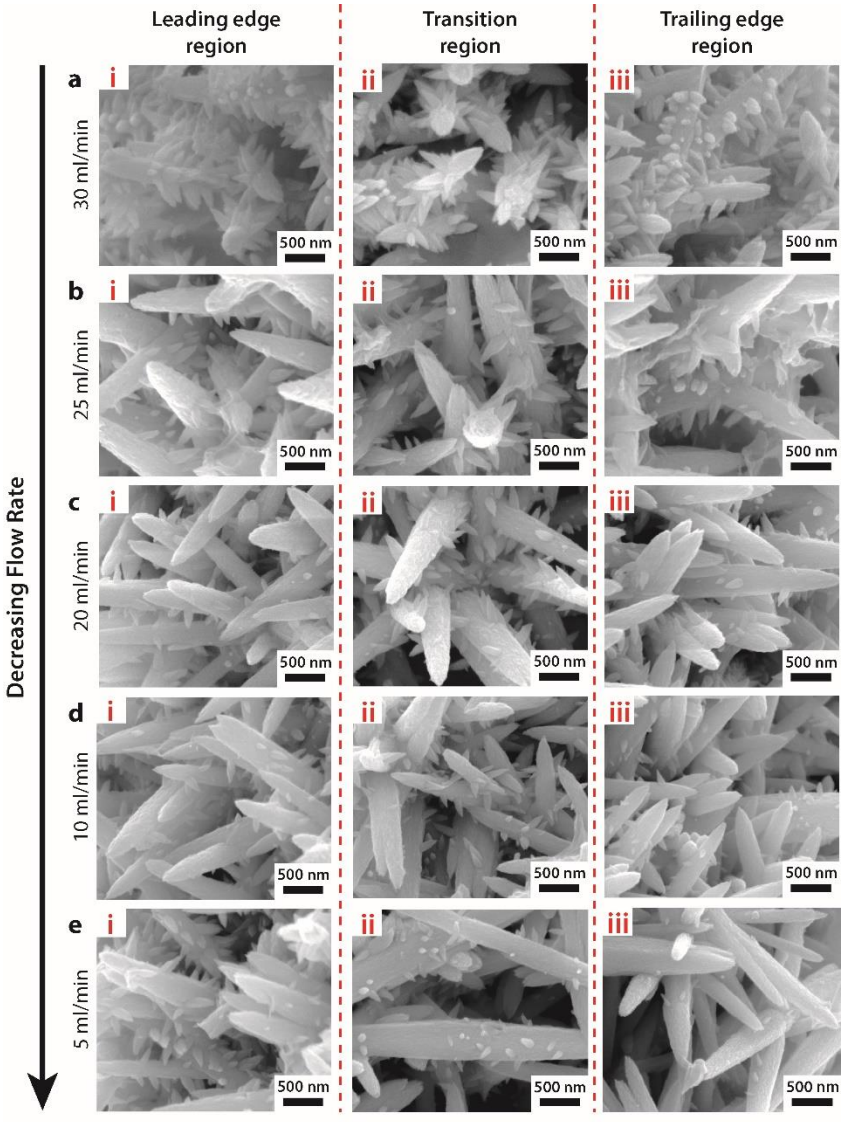

Figure S11. Synthesis of spatially/compositionally variant ZnO mesostructures. (a) SEM images of the NR array with *Cu* doped ZnO branches and magnified images from the LR, TsR, and TR regions. (b) The Atomic % of *Cu* across the filament determined using EDS.

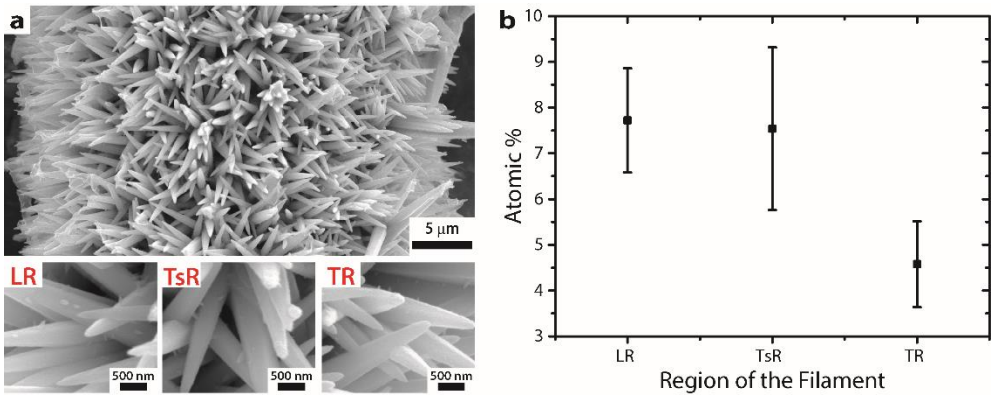

References

1 A. Konda, J. M. Taylor, M. A. Stoller and S. A. Morin, *Lab Chip*, 2015, **15**, 2009-2017.
2 X. N. Wen, W. Z. Wu, Y. Ding and Z. L. Wang, *J. Mater. Chem.*, 2012, **22**, 9469-9476.
3 X. Z. Li, *Microsc. Microanal.*, 2016, **22**, 564-565.
4 F. M. White, *Fluid mechanics*, McGraw-Hill, New York, NY, 6th edn., 2009.
5 H. A. Stone, in *CMOS Biotechnology*, eds. H. Lee, R. M. Westervelt and D. Ham, Springer US, Boston, MA, 2007, DOI: 10.1007/978-0-387-68913-5_2, pp. 5-30.
6 B. N. Rajani, A. Kandasamy and S. Majumdar, *Appl. Math. Model.*, 2009, **33**, 1228-1247.
7 I. V. Markov, *Crystal growth for beginners : fundamentals of nucleation, crystal growth and epitaxy*, World Scientific, Singapore, 2nd edn., 2003.
8 S. A. Morin, M. J. Bierman, J. Tong and S. Jin, *Science*, 2010, **328**, 476-480.
9 W. K. Burton, N. Cabrera and F. C. Frank, *Philos. Trans. R. Soc., A*, 1951, **243**, 299-358.
10 P. Van Cappellen and J.-F. Gaillard, *Rev. Mineral. Geochem.*, 1996, **34**, 335-376.